JGR Oceans

RESEARCH ARTICLE
10.1029/2022JC019509

Observed Structure of an Internal Tide Beam Over the Mid-Atlantic Ridge

Clément Vic[1] **and Bruno Ferron**[1]

[1]University of Brest, CNRS, Ifremer, IRD, Laboratoire d'Océanographie Physique et Spatiale (LOPS), IUEM, Plouzané, France

Key Points:

- An internal tide beam generated by an abyssal hill is observed by a Shipboard Acoustic Doppler Current Profiler through a section over the Mid-Atlantic Ridge
- A linear wave theory quantitatively reconstructs the beam structure, interpreted as the superposition of modal internal tides
- Modes 1–3 are the most energetic but modes 2–6 are the ones that fit best the horizontal structure of modal internal tides

Supporting Information:

Supporting Information may be found in the online version of this article.

Correspondence to:

C. Vic,
clement.vic@ifremer.fr

Citation:

Vic, C., & Ferron, B. (2023). Observed structure of an internal tide beam over the Mid-Atlantic Ridge. *Journal of Geophysical Research: Oceans*, *128*, e2022JC019509. https://doi.org/10.1029/2022JC019509

Received 21 NOV 2022
Accepted 16 JUN 2023

Author Contributions:

Conceptualization: Clément Vic, Bruno Ferron
Data curation: Bruno Ferron
Investigation: Clément Vic, Bruno Ferron
Methodology: Clément Vic, Bruno Ferron
Resources: Clément Vic, Bruno Ferron
Writing – original draft: Clément Vic
Writing – review & editing: Bruno Ferron

Abstract Internal tides are key players in ocean dynamics above mid-ocean ridges. The generation and propagation of internal tides over the Mid-Atlantic Ridge (MAR) have been studied through theoretical and numerical models, as well as through moored, that is, one-dimensional, observations. Yet, observations remain sparse and often restricted to the vertical direction. Here we report on the first two-dimensional in situ observation of an internal tide beam sampled by a shipboard acoustic Doppler current profiler through a vertical section over the MAR. The beam is generated by the interaction of the barotropic tidal current with a supercritical abyssal hill that sits in the rift valley of the MAR. A vertical mode decomposition is carried out to characterize the spatio-temporal variability of the beam. Although the modal content of the velocity field is dominated by modes 1 to 3, higher modes display localized and not persistent bursts of energy. The use of an analytical theory for linear internal waves allows us to rationalize the observed velocity field and interpret it as the superposition of modal waves generated on the hill and propagating in the same direction. The observed beam is qualitatively reconstructed as the superposition of waves of modes 2 to 6. The velocity field was sampled seven times across the same section and displayed qualitatively different patterns, unveiling the complexity of the dynamics above the MAR. A ray tracing of modal waves shows that the refraction by mesoscale currents could explain the observed variability of the tidal beam.

Plain Language Summary In the stratified ocean, the interaction of tidal currents with the seafloor topography generates waves that propagate along and across density layers. Those waves, called internal tides, play important roles in the equilibrium of the ocean. Yet, their fine-scale observations are sparse and uncertainties remain on their lifecycle. Using a shipboard current profiler through a section over the Mid-Atlantic Ridge, we sampled a clear signal of an internal tide beam, a structure whose existence has been unveiled by theories and models but never observed on the Mid-Atlantic Ridge. We use a simple linear theory to characterize the beam and rationalize the observed velocity field, which can be interpreted as the superposition of many waves with distinct spatial structures.

1. Introduction

The interaction of an oscillating flow with topographic structures in a stratified medium generates internal waves. In the stratified ocean, tidal currents interact with the seafloor topography to generate internal waves at tidal frequencies, or internal tides. Internal tides can propagate thousands of kilometers away from their generation sites and they populate the oceans almost ubiquitously (Alford, 2003). Consequently, they have a signature on a vast majority of in situ measurements, at the surface and in the deepest layers (e.g., Johnson et al., 2022; Yu et al., 2019). Internal tides (and internal waves in general) have been investigated for two reasons that were hinted in a seminal review paper (Garrett & Munk, 1979). First, they need to be accurately described to be removed from raw observations in order to isolate the slowly varying state of the ocean. Second, they play a crucial role in the irreversible mixing of water masses. The first point has recently received a regained interest in the context of new satellite missions that unveil the ocean surface topography at unprecedented resolution (Le Guillou et al., 2021; Morrow et al., 2019). The second point has since been confirmed (St. Laurent & Garrett, 2002) and the community now has a clearer view on the lifecycle of internal tides (e.g., reviewed in Whalen et al., 2020; Musgrave et al., 2022), on their global characteristics and interactions within the internal wave continuum (Le Boyer & Alford, 2021; Pollmann, 2020), on the geography of their induced mixing (de Lavergne et al., 2019, 2020) and how this mixing impacts the circulation (e.g., reviewed in de Lavergne et al. (2022)).

Theories for the generation of internal tides in the deep ocean, or barotropic-to-baroclinic energy conversion, are linear and resort to a strong assumption: the slope of internal wave rays must be larger than the slope of the seafloor topography (Garrett & Kunze, 2007). The seafloor slope is then termed subcritical and linear theories describe the generated internal tide field as the superposition of waves with distinct vertical structures, or vertical modes, whose shapes are determined by the profile of the buoyancy frequency N^2. Each mode is associated with a horizontal wavelength, also depending on N^2, the Coriolis frequency f and the tidal frequency ω. Energy distribution throughout the modes depends on the variance of the seafloor topography in each corresponding wavelength (Falahat, Nycander, Roquet, & Zarroug, 2014; St Laurent & Nash, 2004; Vic et al., 2019). If the seafloor topography approaches criticality or becomes supercritical (i.e., its slope is equal to or larger than the slope of internal wave rays), linear theories are not strictly valid and the structure of internal tides is qualitatively different, with energy focusing in beams (Balmforth et al., 2002; Legg & Huijts, 2006). Nonetheless, internal tide beams can also be interpreted as the superposition of many vertical modes (Gerkema, 2001).

The seafloor topography of the Mid-Atlantic Ridge (MAR) is mostly subcritical for semidiurnal tides, and linear theories predict quantitatively well the barotropic-to-baroclinic energy conversion compared to moored observations of energy fluxes (St Laurent & Nash, 2004; Vic, Naveira Garabato, et al., 2018), and results from primitive-equation (hence non linear) regional and global models (Buijsman et al., 2020; Lahaye et al., 2020; Zilberman et al., 2009). However, those models use seafloor topographies that do not, or partially, resolve the ≈10-km scales typical of abyssal hills, which populate slow-spreading mid-ocean ridges (Goff, 2010; Goff & Arbic, 2010) and often feature supercritical slopes (Melet et al., 2013). Taking into account those hills can lead to an increase in the portion of supercritical slopes to 15%, locally (Melet et al., 2013). Hence, we can theoretically expect internal tides to be generated in the form of beams on the MAR. To our knowledge, despite some evidence for the generation of internal tide beams over the MAR from one modelling study (Zilberman et al., 2009, see their Figure 7), no in situ observation of such beams has been reported. Note that, in general, in situ observations of internal tide beams remain sparse as they need closely spaced measurements (e.g., Cole et al., 2009; Lien & Gregg, 2001; Pichon et al., 2013).

Here, we report on an observed internal tide beam generated by an abyssal hill in the rift valley of the MAR. The beam is sampled by a Shipboard Acoustic Doppler Current Profiler (SADCP) that measures the horizontal velocity field through a section that crosses the main axis of an abyssal hill. We use a linear theory for internal wave propagation that allows us to reconstruct the observed pattern of the beam. The paper is organized as follows. Section 2 presents the context of the data collection and the datasets used in the study. Section 3 introduces the methods and Section 4 presents the results. These are discussed in Section 5 and summarized in Section 6.

2. Context and Data

2.1. The MoMARSAT 2022 Cruise

Data were collected by R/V Pourquoi Pas ? during the MoMARSAT cruise on 6–27 June 2022 (Sarradin & Matabos, 2022). The MoMARSAT cruise series provides annual maintenance for the European Multidisciplinary Seafloor and water column Observatory (EMSO) Azores observatory on the Lucky Strike hydrothermal field (Cannat & Sarradin, 2010; Matabos et al., 2022). This seafloor observatory has been operated since 2010 and aims to acquire long time series on hydrothermal and geophysical processes and ecosystems of an active hydrothermal field on the MAR (Figures 1a and 1b).

Most of the ship time was dedicated to servicing the seafloor observatory but during the crew's off-duty time slots (6–8 hr long) we sailed on the section shown in Figure 1b to measure the fine-scale variability of horizontal currents with the SADCP. High-resolution regional models have recently unveiled complex structures of currents in the rift valley of the MAR, featuring density currents, submesoscale processes and internal waves, altogether impacting the dispersal of geochemical material emitted at vent sites (Lahaye et al., 2019; Tagliabue et al., 2022; Vic, Gula, et al., 2018). Yet the rich modelled phenomenology remains to be confirmed by observations from process-oriented cruises, which remain sparse (e.g., Thurnherr et al., 2002; Tippenhauer et al., 2015; Walter et al., 2010). To choose the section with the highest interest, we examined the multibeam bathymetry around Lucky Strike to identify a section that would cross a potential site of strong internal tide generation and could be sailed back and forth in 6–8 hr. The abyssal hill whose main axis is shown by the white dashed line in Figure 1b appeared to be a strong candidate for energetic internal tide generation as its slope reaches 15% and it qualified

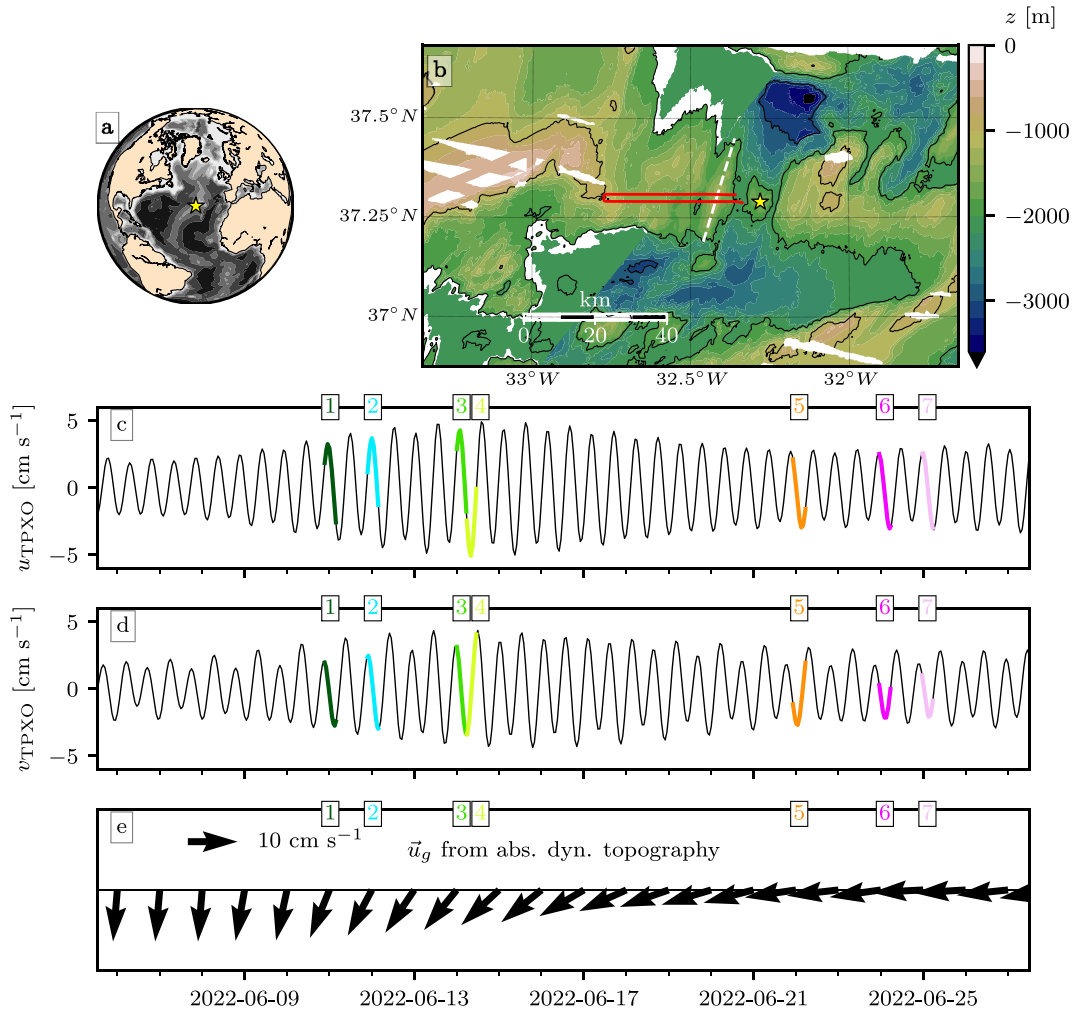

Figure 1. (a) Location of the Lucky Strike hydrothermal vent in the North Atlantic as shown by the yellow star. Bathymetry from a coarsened version of original ETOPO2v2 (W. H. F. Smith & Sandwell, 1997) is shown in gray, with a shade interval of 1,000 m. (b) Multi-beam bathymetry in the rift valley of the Mid-Atlantic Ridge sector around Lucky Strike (yellow star). White areas represent unsampled regions. The red line represents the nominal ship track along which Shipboard Acoustic Doppler Current Profiler (SADCP) data are presented in this study. The dashed white line shows the axis of the abyssal hill from which the internal tide beam emerges. (c and d) Time series of zonal and meridional barotropic tide velocities (u_{TPXO} and v_{TPXO}, respectively) at the Lucky Strike site as derived from the Oregon State University Tidal Prediction Software using TPXO9-atlas. Colored lines show times of SADCP data collection along the seven repeat sections. (e) Time series of the surface geostrophic current derived from absolute dynamic topography measured by satellite altimetry (made available by Copernicus, see text for details). Colored numbers in (c–e) are section crossing numbers.

as supercritical. We repeated the section crossing seven times at different phases of the tidal cycle and spanning spring and neap tides, as shown in time series of the barotropic tidal currents (Figures 1c and 1d). The surface geostrophic currents, derived from satellite altimetry, also varied between the samplings (Figure 1e).

2.2. SADCP Data

The SADCP was a 38-kHz OceanSurveyor narrowband ADCP manufactured by Teledyne RDI. Raw data from the RDI VmDas software were processed using the Cascade Exploitation software v7.2 (Le Bot et al., 2011, www.umr-lops.fr/Technologies/Logiciels/ADCP-de-coque). The SADCP was pinging at 0.25 Hz and data were bin-averaged in 120-s ensembles. The vertical resolution is 24 m and data were available nominally from 54 to 1,518 m depth (bin centers). The ship sailed at 3–4 m s^{-1} so the apparent horizontal resolution of the measurements through a section is 500 m, roughly. Data were cleaned using a series of tests and filters featuring

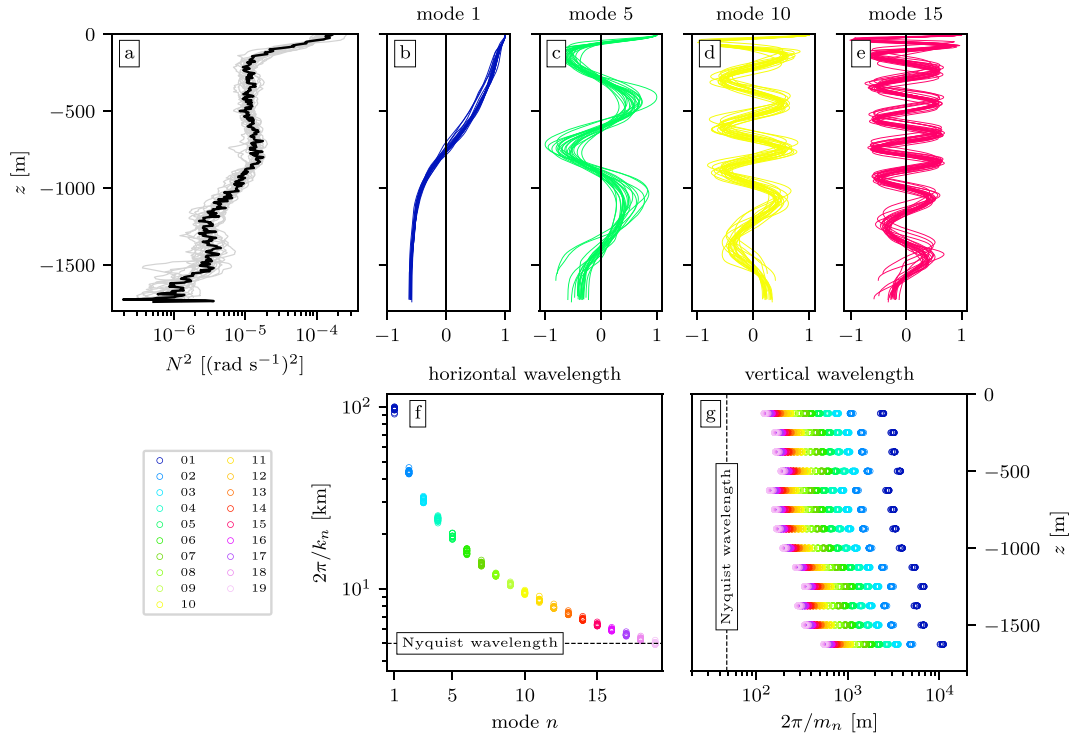

Figure 2. (a) Gray lines show N^2 from 22 Conductivity-Temperature-Depth profiles and the black line is the average from all individual N^2. (b–e) Vertical modes 1, 5, 10, and 15 from individual N^2. (f) Horizontal wavelength of modes 1–19 for the M_2 tide computed from all individual N^2 profiles. (g) Vertical wavelength of modes 1–19 for the M_2 tide computed with a depth interval of 125 m. In (f) and (g), the black dashed line shows the Nyquist wavelength, that is, the minimum wavelength resolved in the observations.

conservative default values (Lherminier et al., 2007) and velocities were further corrected for pitch errors so as to remove biases in the vertical velocities. The expected error using this SADCP configuration was 0.037 m s^{-1}. A cross-comparison of SADCP and lowered-ADCP velocity profiles at CTD stations (Section 2.3) showed a good consistency between those independent measurements.

2.3. Hydrographic Data

We use temperature and salinity profiles from a Conductivity-Temperature-Depth (CTD) probe mounted on a rosette to compute N^2 from the TEOS-10 toolbox (McDougall & Barker, 2011). Overall, 22 casts were performed in the vicinity of Lucky Strike, approximately 10 km east of the easternmost point of the section. N^2 from those profiles is shown in Figure 2a.

2.4. Barotropic Tidal Currents

We compute the barotropic tidal currents in the eight major components (M_2, S_2, K_2, N_2, K_1, O_1, P_1, Q_1) at the Lucky Strike site for the time of the cruise using the Oregon State University Tidal Prediction Software (https://www.tpxo.net/otps) with TPXO9-atlas (Egbert & Erofeeva, 2002). Currents are shown in Figures 1c and 1d.

2.5. Geostrophic Surface Currents

We use the geostrophic surface currents derived from absolute dynamic topography measured by satellite altimetry and made available by the Copernicus Marine Environment Monitoring Service (near-real time L4 product) on a 0.25° grid at a daily frequency. Currents were then linearly interpolated in the middle of the section for the cruise time (Figure 1e). They were also used to perform the ray tracing presented in Section 3.3.

3. Methods

3.1. Vertical Modes

We use the linear theory for internal gravity waves. Internal gravity waves are the solutions of the linearized primitive equations. Assuming a separation of variables in the form $[u(x, y, z, t), v(x, y, z, t) = [U(x, y, t), V(x, y, t)]F(z)$ for horizontal velocity and $w(x, y, z, t) = W(x, y, t)G(z)$ for vertical velocity leads to resolving a Sturm-Liouville problem (we use the same notations as in Chapter 4 in Wunsch (2015)):

$$\frac{\mathrm{d}^2G(z)}{\mathrm{d}z^2} + N^2(z)\gamma^2G(z) = 0, \tag{1}$$

where γ^2 is the separation constant, and with boundary conditions at the surface $G(z = 0) = 0$ and at the bottom $G(z = -h) = 0$. Vertical structures are related through $F(z) = \frac{\rho_0}{\gamma^2}\frac{\mathrm{d}G}{\mathrm{d}z}$. The problem is solved numerically for the 22 profiles of N^2 (Figure 2). The lowest modes are weakly dependent on the details of each individual $N^2(z)$ with zero crossings located at very comparable depths throughout the profiles (Figures 2b and 2c). In contrast, the highest modes are more sensitive to the total depth (there are less data at depth so more uncertainty in N^2) and small-scale wiggles in $N^2(z)$, and zero crossings span larger depth ranges (Figures 2d and 2e).

The modal amplitude of the velocity fields u, v is obtained by projecting the observed fields onto the different modes computed from the averaged N^2 for each vertical profile (Lahaye et al., 2020). This is preferred over resolving a least-square problem, which sometimes leads to unrealistic modal amplitudes into the high modes.

3.2. Observable Wavelengths

The resolution of Equation 1 gives γ^2 for each mode, which is the inverse squared eigenspeed c_n of vertical mode n, that is, the phase speed of a mode-n internal gravity wave. The horizontal wavenumber of mode n is then given by $k_n = \left(\omega^2 - f^2\right)^{1/2}/c_n$. The horizontal wavelength $2\pi/k_n$ for each mode and each N^2 profile is shown in Figure 2f. Mode-1 horizontal wavelength is 90–100 km, in agreement with Ray and Zaron (2016) in this region. The horizontal wavelength decreases with mode number as $1/n$. To reduce the horizontal "grid-scale" noise in the SADCP velocity fields when doing the modal decomposition, we added a horizontal smoothing to the fields with a half-width of two points. Hence, the original apparent resolution is coarsened by a factor of five, from ≈500 m to 2.5 km. The Nyquist wavelength, that is, the smallest wavelength that can sampled, is thus 5 km. It is shown in Figure 2f and intersects the range of estimated mode-19 wavelengths. Mode 19 hence becomes the highest observable mode regarding the horizontal resolution criterion.

We estimated the vertical wavelength of mode n, m_n, through the relation

$$\frac{k_n}{m_n} = \left(\frac{\omega^2 - f^2}{N^2 - \omega^2}\right)^{1/2}. \tag{2}$$

As it intrinsically depends on the local stratification, we estimated m_n at different depths between 125 and 1,725 m with a depth interval of 125 m (Figure 2g). Mode 19 features the shortest wavelength in the pycnocline below 500 m : $m_{19} \approx 150$ m. This is much larger than the Nyquist wavelength, which is 48 m, given the bin width of the SADCP data (24 m, see Section 2.2). Resolving the horizontal wavelength is thus more limiting than resolving the vertical wavelength for observing the highest modes. In the following, we will consider mode 19 as the highest observable mode allowed by the SADCP sampling.

3.3. Ray Tracing

In order to investigate the role of the mesoscale turbulence in the refraction of the tidal beam, we opted for a ray tracing approach, using the algorithm presented in Section 3b in Rainville and Pinkel (2006). The model propagates modal internal waves horizontally from a given generation point, taking into account spatially variable gravity wave speed, planetary vorticity and barotropic mesoscale currents. The gravity wave speed is computed prior to performing the propagation, solving the Sturm-Liouville problem for the stratification derived from the World Ocean Atlas 2018 temperature and salinity (Locarnini et al., 2018; Zweng et al., 2018). Following Rainville and Pinkel (2006), we estimated the barotropic mesoscale currents to have the same direction but half

of the magnitude of the geostrophic currents calculated from sea surface height (Section 2). Also, the mesoscale field is frozen throughout the propagation, which is a weak assumption given the short time scales (<3 days) and distances (<50 km) considered.

3.4. Finescale Parameterization of Turbulent Kinetic Energy Dissipation

Dissipation rates of turbulent kinetic energy along the sections were estimated from a finescale parameterization based on the internal wavefield content measured with the SADCP. We used the Gregg et al. (2003) parameterization, which needs a knowledge of the shear-to-strain ratio R_ω of the internal wavefield. In the absence of concurrent CTD data during SADCP sections to compute an instantaneous R_ω, we used an averaged vertical profile of R_ω computed from the 22 CTD profiles (see Section 2.3) combined with the simultaneous lowered-ADCP profiles obtained from two 300-kHz ADCPs mounted on the rosette frame. Following Gregg (1989), the variance of the vertical shear of the horizontal velocities was obtained from finite differences, here calculated over a length scale of 96 m (two consecutive bins) after having vertically smoothed the velocity with a three-point Hanning filter. This variance estimate is scaled by the corresponding variance of the Garrett and Munk (1975) spectrum.

4. Results

We first show and interpret phenomenologically the raw observations of the horizontal velocity field for one transect (Section 4.1) before interpreting it more quantitatively in light of the theory for linear wave propagation (Section 4.2).

4.1. Observation of the Internal Tide Beam

Figure 3 gives an overview of the sampled velocity field. The ship performed the section in roughly 6 hr (Figure 3a), which thus spans half a semidiurnal cycle, with barotropic tidal currents in opposite direction between the beginning and the end of the transect (Figure 3b). Figures 3c and 3d show the raw baroclinic currents u_{bc}, v_{bc} sampled by the SADCP. Both fields show a clear oblique pattern of enhanced velocity (up to 25 cm s^{-1}) emerging from the top of an abyssal hill situated 30–35 km to the edge of the section, which corresponds to the ship's u-turn (i.e., the origin of the horizontal axis corresponds to the westernmost point of the section). The hill corresponds to the one identified in Figure 1b, which is roughly perpendicular to the ship track. Given that the barotropic tidal ellipse is not much polarized (Figure 3b), we expect the generated waves to propagate in the direction of the largest topographic gradient (Pollmann & Nycander, 2023). This direction is perpendicular to the hill main axis, that is, close to the ship direction. Equivalent of Figure 3 for the six other crossings of the same section are shown in Figures S1–S6 in Supporting Information S1 and are discussed in Section 5.1.

Clues for identifying the oblique pattern as a tidal wave beam are manifold. First, the theoretical beam trajectory, constructed from the depth-dependent beam slope (Equation 2), visually matches the pattern of constant phase for u_{bc} and v_{bc}. Second, the hill slope, from which the beam emerges, is clearly steeper than the beam slope. As identified prior to the sampling, this supercritical slope is thus a strong candidate for generating beam-like patterns of internal tides. Third, the velocity field u_{bc} is antisymmetric with respect to the section edge (Figure 3c), while v_{bc} is symmetric (Figure 3d). This is in agreement with sampling a periodic signal over half a period (6-hr to complete the section), with a phase shift of a quarter of a period between u_{bc} and v_{bc}—this is expected from linear wave theory, as discussed in Section 4.2. Note that here we made the implicit assumption that the internal tides were coherent (phase-locked to the astronomical forcing), which is likely to be valid close to the generation site and in the relatively quiescent mesoscale environment of the MAR (e.g., Figure 1 in Thoppil et al., 2011).

We now investigate the modal content of the velocity field. Overall, the baroclinic velocity field is dominated by the three lowest modes, which together account for about half of the variability in each profile (Figure 3e). However, the modal content varies importantly on small horizontal scales throughout the section with localized bursts of energy into modes 5–15. Those bursts do not seem to extend horizontally over the characteristic horizontal wavelengths of the high-mode internal waves (5–20 km, Figure 2f). This makes those structures difficult to interpret in terms of coherent internal waves.

The time variability of the modal content, assessed between the ship's outbound and inbound, also appears to be important with no clear symmetry with respect to the section westernmost edge. This small-scale variability

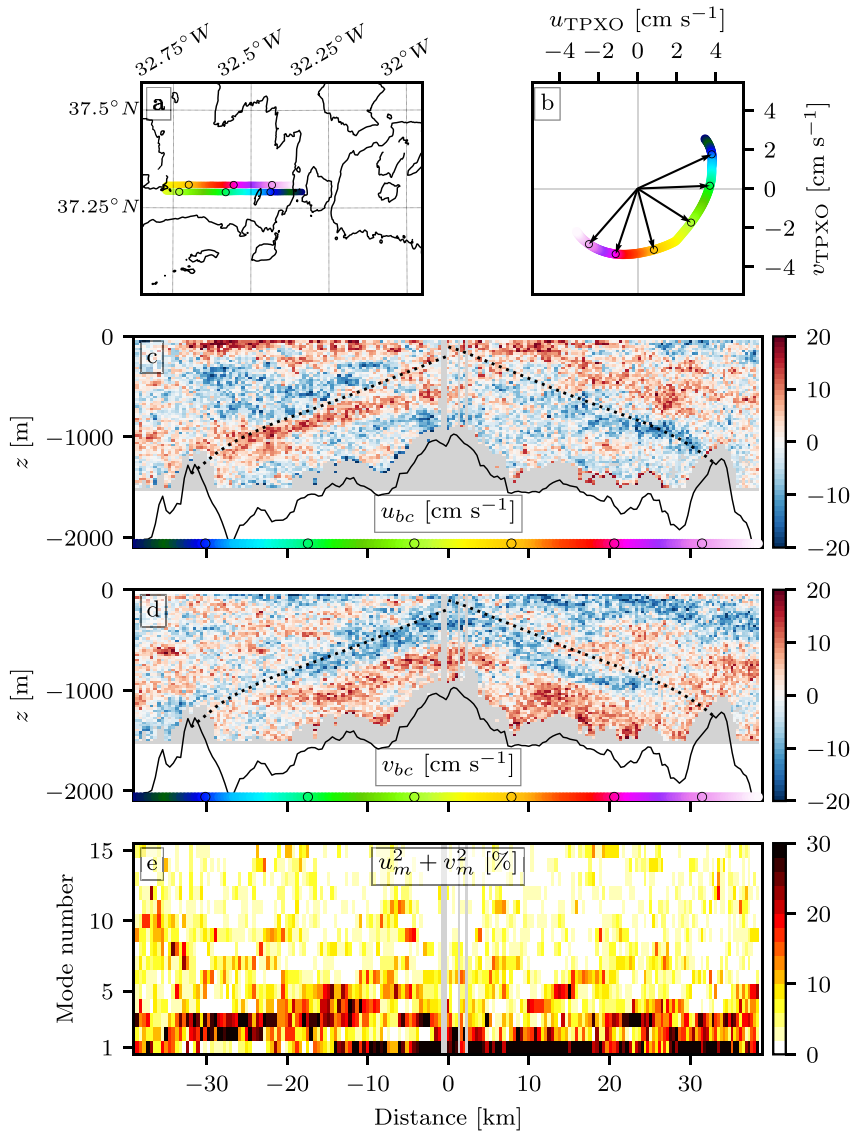

Figure 3. (a) The ship track is shown in colors with one empty circle every hour. Black lines show multibeam bathymetry contours 1,000 and 2,000 m. (b) Barotropic tidal currents from TPXO along the ship track. (c) Zonal and (d) meridional baroclinic currents measured by the ADCP. The black line shows the multibeam bathymetry and dashed lines show analytical tidal beam trajectories. The colored line and empty circles at the bottom of each panel are shown to assess the ship position and barotopic tidal currents along the section, referring to (a and b), respectively. (e) Contribution of modes 1–15 in the energy content for every profile along the transect.

of the modal content in space and time has been represented in the rift valley of the MAR in a high-resolution regional model (Lahaye et al., 2020) but had never been documented with in situ data. It could be interpreted as enhanced energy transfer between modes through topographic scattering (Lahaye et al., 2020). Note that this small-scale variability in the high modes could also be explained by localized variations in N^2 that change the high-mode shapes between neighboring profiles (Figures 2d and 2e). Finally, sources of internal tides are ubiquitous over the MAR and the rapidly changing modal content of the velocity field could be due to waves travelling through the sampled section.

4.2. Analytical Reconstruction of the Beam

In this section, we show that the observed internal wave beam can be rationalized as the superposition of modal internal tides. To do so, we lean on several assumptions. The strongest assumption is that the observed velocity

field is mainly made up of internal tides. In other words, we assume that the low-frequency velocity field composed of large-scale and mesoscale currents can be neglected. We also assume that the stratification is constant in space and time throughout the sampled section, so that the waves' modal structure is constant. The limitations of our results tied to these assumptions are discussed in Section 5.1.

We work in the plane defined by the zonal (x) and vertical (z) directions. In general, a horizontal velocity field can be expressed as $[u(x,z,t), v(x,z,t)] = \sum_n [u_n(x,z,t), v_n(x,z,t)]$. In the specific case of linear internal waves, analytical expressions u_n^a, v_n^a for u_n, v_n can be written as:

$$u_n^a(x,z,t) = U_n\, F_n(z) \exp i(\omega t - k_n x - \phi_n) \tag{3}$$

$$v_n^a(x,z,t) = V_n\, F_n(z) \exp i\left(\omega t - k_n x - \phi_n - \frac{\pi}{2}\right), \tag{4}$$

where U_n, V_n are the modal amplitudes for u_n, v_n, and ϕ_n is the phase at the origin. Other variables have been defined previously. Note that the polarisation relation involves a phase shift between the zonal and meridional velocity fields such that u_n lags behind v_n by a quarter of a period (e.g., chapter 5 in Gerkema and Zimmerman (2008)).

We then proceed as follows. First, for every mode $n \in [1, 19]$, we normalize the observed velocity field u_n^o, v_n^o by their respective maximum through the section. Then, using the exact ship position and time, that is, variables x and t in Equations 3 and 4, and setting $U_n = V_n = 1$, we seek the phase ϕ_n that maximizes the correlation between (u_n^o, v_n^o) and (u_n^a, v_n^a). In practice, we compute the correlation between observed and analytical fields for $\phi_n \in [0, 2\pi]$ with a phase step of $\pi/32$. Second, if the best correlation is greater than 0.35, we consider that the observed signal can actually be interpreted as an internal wave of mode n and keep it for building the total field. The threshold of 0.35 is of course rather arbitrary but is motivated by (a) some literature in sciences that strongly resort to statistics that qualify a correlation >0.35 (or 0.30) as "moderate" (e.g., Ratner, 2009; Taylor, 1990); and (b) a posteriori good agreement between the observed and analytical fields. Third, the total field is reconstructed by summing the modes that have been retained weighted by their observed amplitudes, that is, U_n, V_n computed from observations.

The analytical field that best fits the observed field for mode 5 is shown as an example in Figure 4. Qualitatively, the observed mode-5 velocity field (u_5^o, v_5^o, Figures 4a and 4c) resembles a mode-5 internal tide. Indeed, a horizontal wavelength slightly smaller than 20 km clearly emerges from the abyssal hill, which is consistent with the theoretical mode-5 wavelength of a semidiurnal internal tide (Figure 2f). Note that the Doppler shift induced by the ship movement would increase the apparent wavelength in the outbound (going in the direction of the wave) and decrease it in the inbound. This is obvious in the analytical fields (Figures 4b and 4d) but not so clear in the observed fields (Figures 4a and 4c). Despite some small-scale differences—observed signals are sometimes unexpectedly damped, which show up as white bands in some profiles—the general patterns of the analytical fields match remarkably well the observed fields. This is confirmed by the two-dimensional histograms of observed versus analytical fields (Figures 4e and 4f) and the correlation coefficients between fields ($r = 0.66$ and $r = 0.71$ for the zonal and meridional velocities, respectively).

The observed energy in each mode averaged over the section, $U_n^2 + V_n^2$, is shown in Figure 5. As already outlined in Section 4.1 and hinted in Figure 3e, the first three modes dominate. There is a gradual decrease of energy throughout the modes as they increase from 4 to 19. The best correlation r_n between observed and analytical fields for mode n is also shown in Figure 5. Interestingly, there is no clear link between $U_n^2 + V_n^2$ and r_n. For example, mode 1 is the most energetic mode but the best fit between the analytical wave and the observed field is not good ($r_1 = 0.26$). This means that the mode-1 velocity field is poorly explained by a semidiurnal internal wave structure. Instead, it could be associated with a surface-intensified balanced structure, such as a front or a mesoscale eddy, whose vertical structure is generally well represented by the barotropic and first baroclinic modes (e.g., K. S. Smith & Vallis, 2001). Recent deepglider measurements in the North Atlantic highlighted that mesoscale eddies are dominated by the first baroclinic mode (Steinberg & Eriksen, 2022). Modes 2–6 feature $r_n > 0.35$ and can reasonably well be interpreted as linear internal waves. Together they account for almost half (47.0%) of the energy into modes 1–19. On the contrary, modes 7–19 all feature $r_n \leq 0.26$ and cannot be interpreted as linear internal waves. Reasons could be manifold. For example, they are by nature more unstable as they feature larger vertical shear, hence are less persistent and more difficult to observe. Also, as already discussed, their structure depends more on small-scale variations in N^2 than the structure of low modes. In consequence, the velocity field

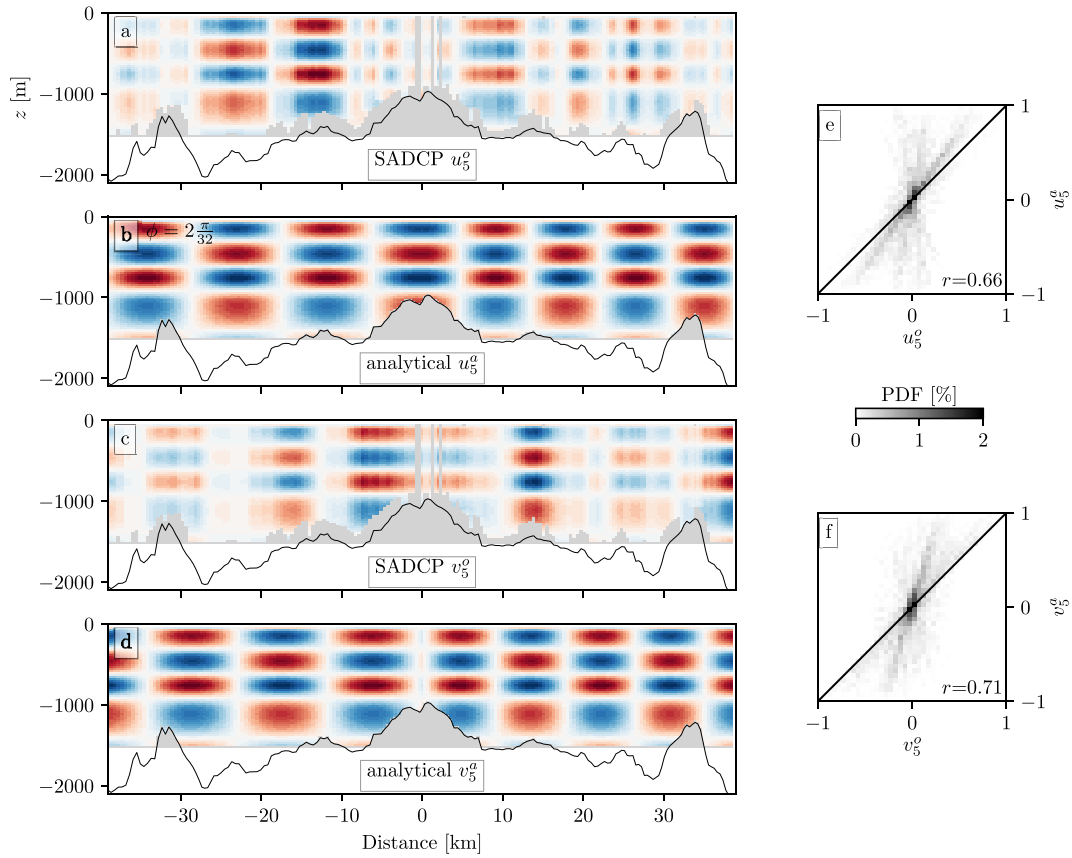

Figure 4. (a) Observed and (b) analytical mode-5 zonal velocity for the phase that maximizes the correlation between observed and analytical fields. (c and d) are the same for the meridional velocity. Velocity fields have been normalized and span the interval [−1; 1] from blue to red. (e and f) are the two-dimensional histograms of observed versus analytical fields for zonal and meridional velocity, respectively. The correlation between fields is given at the bottom right.

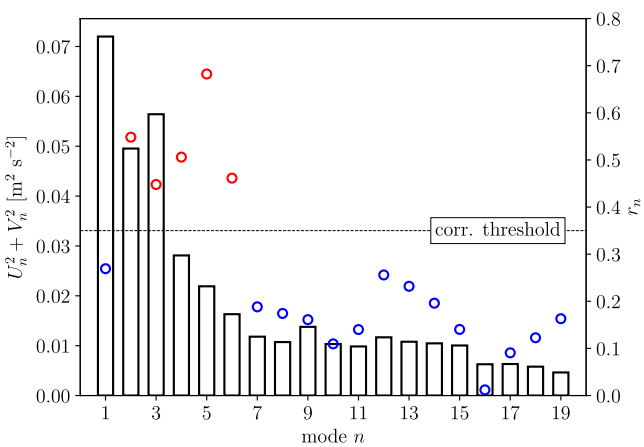

Figure 5. Bars represent energy in each mode averaged through the section and circles represent the correlation between observed and analytical velocity fields for each mode. Circles are red above the correlation threshold (equal to 0.35, black dashed line) and blue below the threshold.

a mode-n wave could be cast into a mode $n \pm 1$ across neighboring profiles if N^2 changes significantly, breaking the apparent steadiness of the field.

Finally, the reconstructed analytical field (u^a, v^a) is compared to the observed field (u^o, v^o) that consists of the modes that have been retained (modes 2–6, Figure 6). The overall velocity structure bears the strong footprint of the beam from the raw section (Figure 3). The observed phase shift for u versus apparent phase steadiness for v between the outbound and the inbound is nicely reproduced in the analytical field. Visually, the vertical structure of the analytical field best fits to observations close to the abyssal hill and the fit degrades with the distance from the hill. This could be interpreted as a decoherence of the waves as they propagate away from the generation site, or as an effect of topographic scattering along their path, which transfers energy to higher modes, hence changing the local amplitude of each mode and the summed structure. The two-dimensional histograms of observed versus analytical fields reveal close agreements between both fields (Figures 6e and 6f). In addition, the correlation coefficients ($r = 0.61$ for u^o vs. u^a and $r = 0.53$ for v^o vs. v^a) give confidence in the fact that the observed beam can actually be interpreted as the superposition of internal wave modes (Gerkema, 2001).

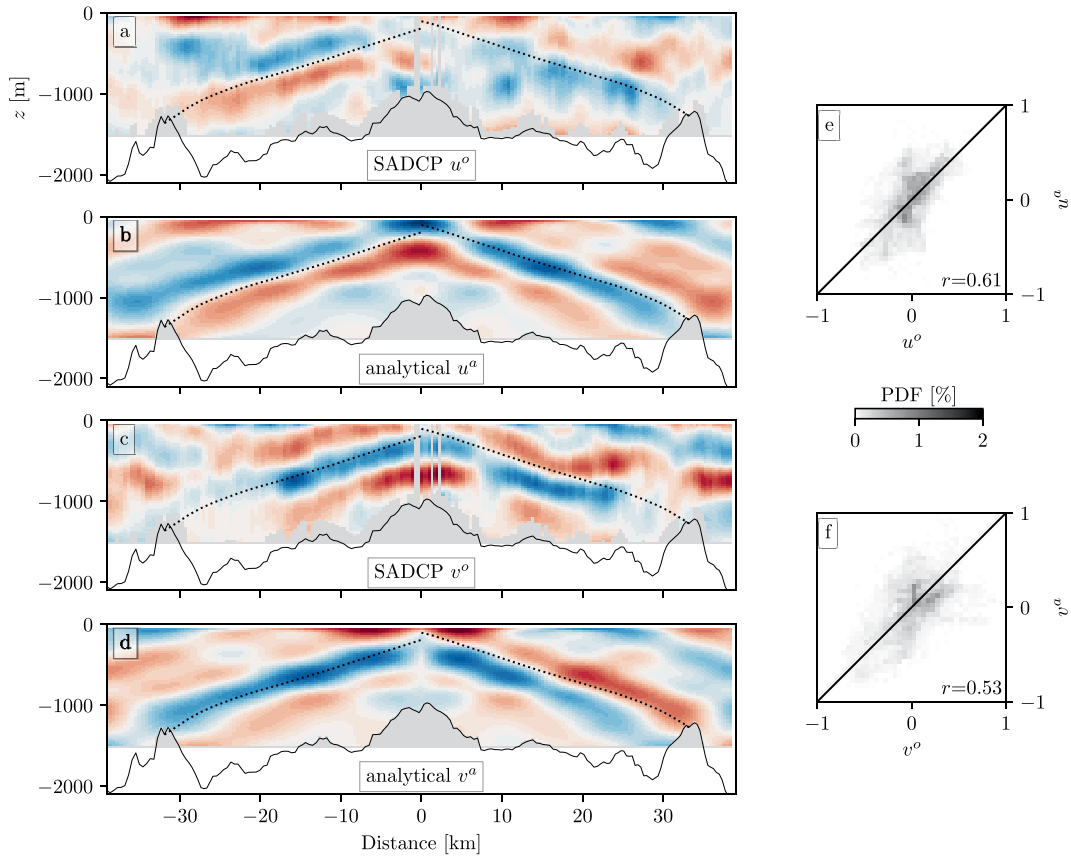

Figure 6. (a) Observed and (b) best estimate analytical zonal velocity. Only modes featuring an observed versus analytical correlation greater than 0.35 have been included—see text. (c and d) are the same for meridional velocity. Velocity fields have been normalized and span the interval [−1; 1] from blue to red. (e and f) are the two-dimensional histograms of observed versus analytical fields for zonal and meridional velocity, respectively. The correlation between fields is given at the bottom right.

5. Discussion

5.1. On the Beam Variability

We sampled the same section seven times, across different phases of the tidal cycle, during spring and neap tides, and throughout a changing surface-intensified geostrophic velocity field (Figures 1c–1e). We repeated the same quantitative analysis as described in Section 4.2 to all sections. Main results are summarized in Table 1.

Among the seven crossings, the first two show qualitatively similar velocity fields (Figure 3 and Figure S1 in Supporting Information S1). This is to be expected as the crossings occurred on the same phase of the barotropic

Table 1
Section Number, Modes Featuring $r_n > 0.35$, Fraction of Energy in the Modes That Feature $r_n > 0.35$, and Correlation Between Reconstructed Fields u^o and u^a, and v^o and v^a, Respectively

Section#	Modes feat. $r_n > 0.35$	$\sum_{r_n>0.35}(U_n^2 + V_n^2)$ (%)	corr. u^o, u^a	corr. v^o, v^a
1	2,3,4,5,6	47.0%	0.61	0.53
2	2,3,4,5,6	43.7%	0.56	0.60
3	3	16.5%	0.54	0.67
4	1,3,5	54.9%	0.71	0.73
5	2	6.1%	0.47	0.71
6	2,3	24.1%	0.58	0.31
7	2,3,5	27.7%	0.61	0.48

tide and at 24 hr interval, so the mesoscale field had not changed much (Figures 1c–1e). Results from the analysis are very comparable for those sections (Table 1).

The third crossing also occurred on a very similar phase of the barotropic tide but 3 days later. The velocity field shows similarities in terms of phase but the modal structure is different, with a strong dominance of modes 1 and 3 (Figure S2 in Supporting Information S1). However, mode 1 does not match a wave structure, so the reconstruction shows a poor agreement (Table 1). We could be reaching the limits of the method here. Indeed, it could be that the mode-1 velocity field is composed of balanced mesoscales and wave signals in comparable proportions, but the method does not permit to disentangle their respective contributions.

The fourth crossing occurred on the opposite phase of the barotropic tide and so is the phase of the baroclinic velocity signal as compared to the first three crossings (Figure S3 in Supporting Information S1). The mode-1 velocity field overwhelms the energy content (Figure S3e in Supporting Information S1) and matches a wave pattern, so the overall fraction of energy represented by internal wave modes is high (modes 1, 3 and 5 represent 54.9%, Table 1), despite the small contributions of modes 3 and 5. Consequently, the summed contribution of the three modes is also dominated by mode 1 and the beam structure is not as clear as for the first three crossings (not shown).

The velocity fields of the last three crossings, performed between eight and 11 days after the fourth crossing, are qualitatively more difficult to interpret in terms of beams (Figures S4–S6 in Supporting Information S1). In particular, the theoretical slope of the beam is much steeper than the slope visually inferred from the observed velocity field. In agreement with this poor visual match, the analysis showed that (a) only a few modes featured $r_n > 0.35$, and (b) that the sum of those modes represented a small fraction of the energy of the total signal (between 6.1% and 27.7%, Table 1).

To sum up, the first four crossings were performed throughout a tight time window and visually display a marked beam structure. This is quantitatively backed up by the modal analysis and reconstruction (except for the third crossing). On the opposite, the last three crossings, also performed throughout a tight time window but 8 days later, do not show a marked beam structure. The qualitative difference between the two groups of crossings could be simply rooted in the spring-neap tidal cycle. The first four crossings were performed close to spring tides whereas the last three were performed closer to neap tides (Figures 1c and 1d). Consequently, the generated beams would be weaker for the second bunch—there is a factor of 4–5 increase in barotropic-to-baroclinic energy conversion during spring tide as compared to neap tide over the MAR (Vic et al., 2021)—and would dissipate more quickly. Another potential cause of the difference could come from different refraction of the beam by the mesoscale circulation (e.g., Rainville & Pinkel, 2006; Zaron & Egbert, 2014), which changed significantly between the beginning and the end of the cruise (Figure 1e).

To further investigate this refraction effect, we used a ray tracing approach that takes into account the geographically variable stratification, planetary vorticity and background mesoscale currents (method is presented in Section 3.3). We performed a ray tracing of synthetic mode-1 to mode-10 internal tides generated in the middle of the abyssal hill main axis with an initial direction of propagation perpendicular to the ridge axis. We performed two simulations using the geostrophic velocity fields derived from satellite altimetry at the beginning (11 June 2022) and at the end (23 June 2022) of the cruise. Results are presented in Figure 7. They show that toward the beginning of the cruise, the waves were more refracted than toward the end. This is due to a stronger mesoscale field (typical velocities of $\approx$20 cm s^{-1} vs. $\approx$10 cm s^{-1}) and a larger angle between the mesoscale velocity field and the original direction of the beam. During the first crossings, the mesoscale field refracted the rays southwestward, giving the rays a dominating westward direction (azimuth often between 265° and 275°, Figure 7a), which is the direction we sailed in. During the last crossings, the rays were less refracted and featured an azimuth greater than 275° (Figure 7b). Hence, the beam was likely to be more accurately sampled at the beginning of the cruise when the waves were more refracted but aligned with the ship's direction. Note that changing the initial location of the synthetic waves does not impact qualitatively the trajectories.

5.2. Turbulent Kinetic Energy Dissipation

Internal tides dissipate their energy through many mechanisms (Whalen et al., 2020). In the deep ocean, away from continental slopes, the two dominant mechanisms are presumably wave-wave interactions and topographic scattering, both leading to a direct energy cascade and wave breaking (de Lavergne et al., 2019, 2020; Lahaye et al., 2020; Onuki & Hibiya, 2018; Wang et al., 2021). Those mechanisms are challenging to quantify and disentangle using in situ measurements, and, to rationalize observed energy dissipation patterns, efforts have

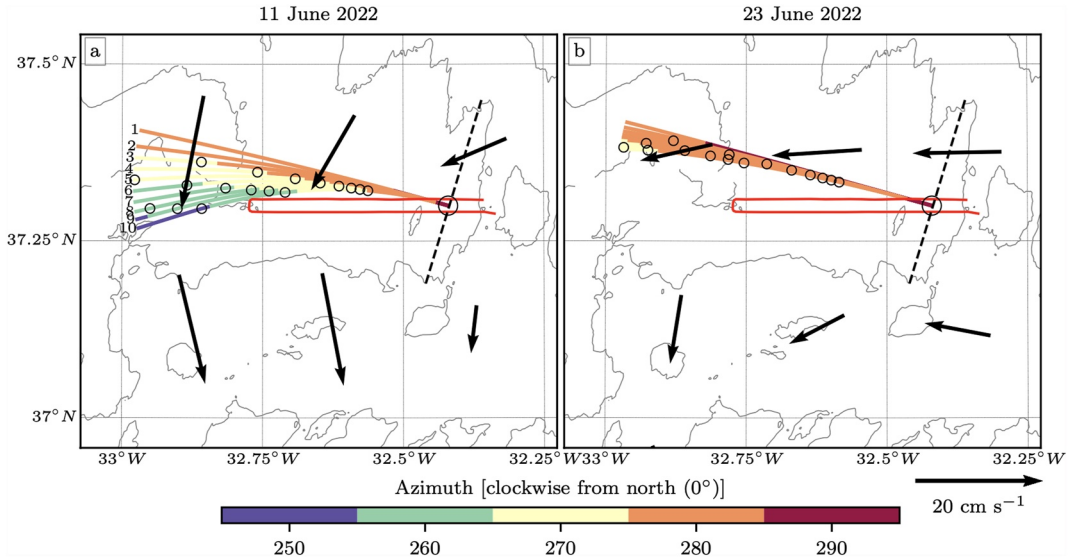

Figure 7. Ray tracing of modal internal tides generated in the middle of the abyssal hill whose principal axis is shown by the dashed black line, and using the background geostrophic velocity fields of (a) 11 June 2022 and (b) 23 June 2022 represented by the black arrows. The initial direction of propagation is taken to be perpendicular to the abyssal hill. Trajectories are shown by the colored lines whose label in (a) corresponds to mode number 1 to 10. Colors represent the azimuth of each ray, clockwise from north (270° is west). Initial position is shown by the large circle and daily positions are shown by the small circles. The thin gray lines represent the multibeam bathymetry with an interval of 1,000 m. The red line represents the nominal ship track.

focused on linking the modal content of internal tide fields (as opposed to considering beams) to local energy dissipation (e.g., Falahat, Nycander, Roquet, Thurnherr, & Hibiya, 2014; Vic, Naveira Garabato et al., 2018; St Laurent & Nash, 2004; St. Laurent & Garrett, 2002; Vic et al., 2019).

We computed kinetic energy dissipation ε through the section using a finescale parameterization (Figure 8, method in Section 3.4). The overall range of ε matches the typical range of dissipation inferred nearby from microstructure measurements of velocity shear (Figure 5 in Ferron et al., 2023). Enhanced dissipation patterns (ε reaching 10^{-8} W kg^{-1}) seem to parallel the theoretical beam trajectories. As the beam is intrinsically composed of several waves, this observation points out to wave-wave interactions as the most plausible mechanism leading to energy dissipation within the beam. In the other crossings that feature a weaker beam, patterns of ε are noisier and more difficult to interpret (not shown). Note that enhanced energy dissipation within tidal beams has been previously highlighted (Cole et al., 2009; Lien & Gregg, 2001). In the specific case of a very energetic beam in a coastal region, dissipation was attributed to shear mixing (Lien & Gregg, 2001).

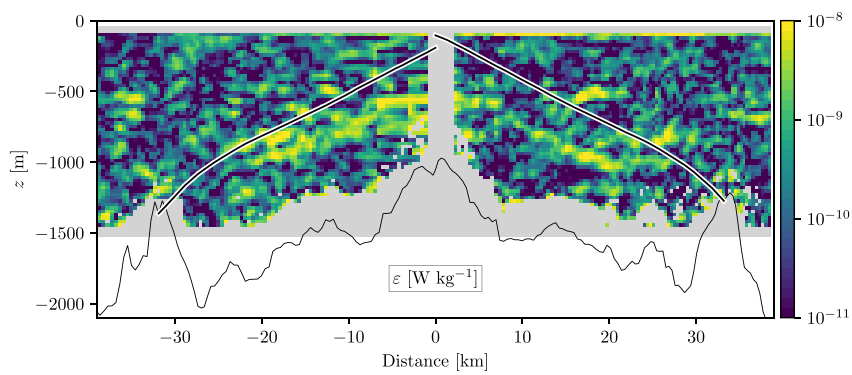

Figure 8. Turbulent kinetic energy dissipation ε inferred from a finescale parameterization (Section 3.4) computed from the velocity field presented in Figures 3c and 3d. Black lines framed in white show analytical tidal beam trajectories.

6. Summary

In summary, we sampled horizontal currents with an SADCP through a 40-km section in the rift valley of the MAR, back and forth, seven times. Four crossings revealed the very clear signal of an internal tide beam that was generated by the interaction of the semidiurnal barotropic tide with a supercritical abyssal hill. Using a linear theory for internal wave structure and propagation, we rationalized the observed field and interpreted the beam as the superposition of waves of modes 2–6. The beam was much weaker in the other crossings, and the strong variability of the velocity field across the seven sections remains unexplained. We speculate that the variability of the barotropic tidal forcing (spring-neap cycle) and the refraction of the waves by the changing mesoscale circulation are playing a role, both in the intensity of the generated beam and in the quality of the sampling. A finescale parameterization of turbulent kinetic energy dissipation revealed enhanced patches of energy dissipation within the beam, highlighting the potential importance of the beam structure for sustaining mixing within the water column.

Finally, standard SADCPs have been routinely used to investigate the large-scale and mesoscale circulation (Section 3 in Rossby, 2016), and our study hints a potential widening of their scope through the capacity of fine-scale sampling internal waves. Nonetheless, our observations also highlighted the complexity of physical processes occurring over the MAR. We believe they deserve a sustained network of moored apparatus to be deeply studied—see recommendations in Matabos et al. (2022, box 2) and Yang et al. (2021) for an innovative observational setup dedicated to investigate deep-sea turbulence.

Data Availability Statement

SADCP data are freely available online (Sarradin & Matabos, 2022). LADCP and CTD data are freely available online (Ferron et al., 2022). TPXO9-atlas barotropic tide currents were made available by Dr. Svetlana Erofeeva who was contacted through https://www.tpxo.net/tpxo-products-and-registration. Geostrophic surface currents from absolute dynamic topography were downloaded from the Copernicus Marine Environment Monitoring Service (near-real time L4 product, Copernicus Marine Service, 2022).

Acknowledgments
B. F. is supported by the Centre National de la Recherche Scientifique (CNRS) and C. V. is supported by the Institut Français de Recherche pour l'Exploitation de la Mer (Ifremer). We thank the captain and crew of R/V Pourquoi Pas ? the chief scientists, P.-M. Sarradin and M. Matabos, and CTD operator S. Leizour for the smooth data collection during the MoMARSAT 2022 cruise. EMSO-Azores is part of the European network EMSO ERIC (European Multidisciplinary Seafloor and water column Observatory, http://emso.eu/), supported in France by the Research Infrastructure (MESR) EMSO-FR, which is managed by an Ifremer-CNRS collaboration. We thank L. Rainville for sharing his code for the ray tracing in Figure 7. We thank the two reviewers for their constructive criticism and valuable suggestions.

References

Alford, M. H. (2003). Redistribution of energy available for ocean mixing by long-range propagation of internal waves. *Nature*, *423*(6936), 159–162. https://doi.org/10.1038/nature01628

Balmforth, N., Ierley, G., & Young, W. (2002). Tidal conversion by subcritical topography. *Journal of Physical Oceanography*, *32*(10), 2900–2914. https://doi.org/10.1175/1520-0485(2002)032<2900:tcbst>2.0.co;2

Buijsman, M. C., Stephenson, G. R., Ansong, J. K., Arbic, B. K., Green, J. M., Richman, J. G., et al. (2020). On the interplay between horizontal resolution and wave drag and their effect on tidal baroclinic mode waves in realistic global ocean simulations. *Ocean Modelling*, *152*, 101656. https://doi.org/10.1016/j.ocemod.2020.101656

Cannat, M., & Sarradin, P.-M. (2010). MoMARSAT: Monitoring the Mid-Atlantic Ridge. https://doi.org/10.18142/130

Cole, S., Rudnick, D., Hodges, B., & Martin, J. (2009). Observations of tidal internal wave beams at Kauai Channel, Hawaii. *Journal of Physical Oceanography*, *39*(2), 421–436. https://doi.org/10.1175/2008JPO3937.1

Copernicus Marine Service (2022). Global ocean gridded L4 sea surface heights and derived variables NRT. [Dataset]. https://doi.org/10.48670/moi-00149

de Lavergne, C., Falahat, S., Madec, G., Roquet, F., Nycander, J., & Vic, C. (2019). Toward global maps of internal tide energy sinks. *Ocean Modelling*, *137*, 52–75. https://doi.org/10.1016/j.ocemod.2019.03.010

de Lavergne, C., Groeskamp, S., Zika, J., & Johnson, H. L. (2022). The role of mixing in the large-scale ocean circulation. In *Ocean mixing* (pp. 35–63). Elsevier. https://doi.org/10.1016/B978-0-12-821512-8.00010-4

de Lavergne, C., Vic, C., Madec, G., Roquet, F., Waterhouse, A., Whalen, C., et al. (2020). A parameterization of local and remote tidal mixing. *Journal of Advances in Modeling Earth Systems*, *12*(5). https://doi.org/10.1029/2020MS002065

Egbert, G. D., & Erofeeva, S. Y. (2002). Efficient inverse modeling of barotropic ocean tides. *Journal of Atmospheric and Oceanic Technology*, *19*(2), 183–204. https://doi.org/10.1175/1520-0426(2002)019⟨0183:EIMOBO⟩2.0.CO;2

Falahat, S., Nycander, J., Roquet, F., Thurnherr, A. M., & Hibiya, T. (2014). Comparison of calculated energy flux of internal tides with microstructure measurements. *Tellus*, *66*(1), 23240. https://doi.org/10.3402/tellusa.v66.23240

Falahat, S., Nycander, J., Roquet, F., & Zarroug, M. (2014). Global calculation of tidal energy conversion into vertical normal modes. *Journal of Physical Oceanography*, *44*(12), 3225–3244. https://doi.org/10.1175/JPO-D-14-0002.1

Ferron, B., Bouruet Aubertot, P., Cuypers, Y., & Vic, C. (2023). Removing biases in oceanic turbulent kinetic energy dissipation rate estimated from microstructure shear data. *Journal of Atmospheric and Oceanic Technology*, *40*(1), 129–139. https://doi.org/10.1175/JTECH-D-22-0035.1

Ferron, B., Vic, C., & Leizour, S. (2022). CTD and LADCP data from the MomarSat 2022 cruise. [Dataset]. https://doi.org/10.17882/94681

Garrett, C., & Kunze, E. (2007). Internal tide generation in the deep ocean. *Annual Review of Fluid Mechanics*, *39*(1), 57–87. https://doi.org/10.1146/annurev.fluid.39.050905.110227

Garrett, C., & Munk, W. (1975). Space-time scales of internal waves: A progress report. *Journal of Geophysical Research*, *80*(3), 291–297. https://doi.org/10.1029/jc080i003p00291

Garrett, C., & Munk, W. (1979). Internal waves in the ocean. *Annual Review of Fluid Mechanics*, *11*(1), 339–369. https://doi.org/10.1146/annurev.fl.11.010179.002011

Gerkema, T. (2001). Internal and interfacial tides: Beam scattering and local generation of solitary waves. *Journal of Marine Research*, *59*(2), 227–255. https://doi.org/10.1357/002224001762882646

Gerkema, T., & Zimmerman, J. (2008). *An introduction to internal waves*. Lecture Notes, Royal NIOZ. Retrieved from https://www.vliz.be/imisdocs/publications/ocrd/60/307760.pdf

Goff, J. A. (2010). Global prediction of abyssal hill root-mean-square heights from small-scale altimetric gravity variability. *Journal of Geophysical Research*, *115*(B12), B12104. https://doi.org/10.1029/2010JB007867

Goff, J. A., & Arbic, B. K. (2010). Global prediction of abyssal hill roughness statistics for use in ocean models from digital maps of paleo-spreading rate, paleo-ridge orientation, and sediment thickness. *Ocean Modelling*, *32*(1–2), 36–43. https://doi.org/10.1016/j.ocemod.2009.10.001

Gregg, M. (1989). Scaling turbulent dissipation in the thermocline. *Journal of Geophysical Research*, *94*(C7), 9686–9698. https://doi.org/10.1029/jc094ic07p09686

Gregg, M., Sanford, T. B., & Winkel, D. P. (2003). Reduced mixing from the breaking of internal waves in equatorial waters. *Nature*, *422*(6931), 513–515. https://doi.org/10.1038/nature01507

Johnson, G. C., Whalen, C. B., Purkey, S. G., & Zilberman, N. (2022). Serendipitous internal wave signals in deep Argo data. *Geophysical Research Letters*, *49*(7), e2022GL097900. https://doi.org/10.1029/2022GL097900

Lahaye, N., Gula, J., & Roullet, G. (2020). Internal tide cycle and topographic scattering over the North Mid-Atlantic Ridge. *Journal of Geophysical Research: Oceans*, *125*(12), e2020JC016376. https://doi.org/10.1029/2020JC016376

Lahaye, N., Gula, J., Thurnherr, A. M., Reverdin, G., Bouruet-Aubertot, P., & Roullet, G. (2019). Deep currents in the rift valley of the North Mid-Atlantic Ridge. *Frontiers in Marine Science*, *6*, 597. https://doi.org/10.3389/fmars.2019.00597

Le Bot, P., Kermabon, C., Lherminier, P., & Gaillard, F. (2011). CASCADE V6.1: Logiciel de validation et de visualisation des mesures ADCP de coque (Tech. Rep.). Retrieved from https://archimer.ifremer.fr/doc/00342/45285/

Le Boyer, A., & Alford, M. H. (2021). Variability and sources of the internal wave continuum examined from global moored velocity records. *Journal of Physical Oceanography*, *51*(9), 2807–2823. https://doi.org/10.1175/JPO-D-20-0155.1

Legg, S., & Huijts, K. M. (2006). Preliminary simulations of internal waves and mixing generated by finite amplitude tidal flow over isolated topography. *Deep-Sea Research II*, *53*(1), 140–156. https://doi.org/10.1016/j.dsr2.2005.09.014

Le Guillou, F., Lahaye, N., Ubelmann, C., Metref, S., Cosme, E., Ponte, A., et al. (2021). Joint estimation of balanced motions and internal tides from future wide-swath altimetry. *Journal of Advances in Modeling Earth Systems*, *13*(12), e2021MS002613. https://doi.org/10.1029/2021MS002613

Lherminier, P., Mercier, H., Gourcuff, C., Alvarez, M., Bacon, S., & Kermabon, C. (2007). Transports across the 2002 Greenland-Portugal Ovide section and comparison with 1997. *Journal of Geophysical Research*, *112*(C7), C07003. https://doi.org/10.1029/2006JC003716

Lien, R.-C., & Gregg, M. (2001). Observations of turbulence in a tidal beam and across a coastal ridge. *Journal of Geophysical Research*, *106*(C3), 4575–4591. https://doi.org/10.1029/2000jc000351

Locarnini, R., Mishonov, A., Baranova, O., Boyer, T., Zweng, M., Garcia, H., et al. (2018). *World Ocean Atlas 2018, volume 1: Temperature* (Vol. 81, p. 52). NOAA Atlas NESDIS. Retrieved from https://data.nodc.noaa.gov/woa/WOA18/DOC/woa18_vol1.pdf

Matabos, M., Barreyre, T., Juniper, S. K., Cannat, M., Kelley, D., Alfaro-Lucas, J. M., et al. (2022). Integrating Multidisciplinary Observations in Vent Environments (IMOVE): Decadal progress in deep-sea observatories at hydrothermal vents. *Frontiers in Marine Science*, *660*. https://doi.org/10.3389/fmars.2022.866422

McDougall, T. J., & Barker, P. M. (2011). Getting started with TEOS-10 and the Gibbs Seawater (GSW) oceanographic toolbox (Vol. *127*).

Melet, A., Nikurashin, M., Muller, C., Falahat, S., Nycander, J., Timko, P. G., et al. (2013). Internal tide generation by abyssal hills using analytical theory. *Journal of Geophysical Research: Oceans*, *118*(11), 6303–6318. https://doi.org/10.1002/2013JC009212

Morrow, R., Fu, L.-L., Ardhuin, F., Benkiran, M., Chapron, B., Cosme, E., et al. (2019). Global observations of fine-scale ocean surface topography with the Surface Water and Ocean Topography (SWOT) mission. *Frontiers in Marine Science*, *6*, 232. https://doi.org/10.3389/fmars.2019.00232

Musgrave, R., Pollmann, F., Kelly, S., & Nikurashin, M. (2022). The lifecycle of topographically-generated internal waves. In *Ocean mixing* (pp. 117–144). Elsevier. https://doi.org/10.1016/B978-0-12-821512-8.00013-X

Onuki, Y., & Hibiya, T. (2018). Decay rates of internal tides estimated by an improved wave–wave interaction analysis. *Journal of Physical Oceanography*, *48*(11), 2689–2701. https://doi.org/10.1175/JPO-D-17-0278.1

Pichon, A., Morel, Y., Baraille, R., & Quaresma, L. (2013). Internal tide interactions in the Bay of Biscay: Observations and modelling. *Journal of Marine Systems*, *109*, S26–S44. https://doi.org/10.1016/j.jmarsys.2011.07.003

Pollmann, F. (2020). Global characterization of the ocean's internal wave spectrum. *Journal of Physical Oceanography*, *50*(7), 1871–1891. https://doi.org/10.1175/JPO-D-19-0185.1

Pollmann, F., & Nycander, J. (2023). Resolving the horizontal direction of internal tide generation: Global application for the M_2-tide's first mode. *Journal of Physical Oceanography*, *53*(5), 1251–1267. in press. https://doi.org/10.1175/JPO-D-22-0144.1

Rainville, L., & Pinkel, R. (2006). Propagation of low-mode internal waves through the ocean. *Journal of Physical Oceanography*, *36*(6), 1220–1236. https://doi.org/10.1175/JPO2889.1

Ratner, B. (2009). The correlation coefficient: Its values range between +1/-1, or do they? *Journal of Targeting, Measurement and Analysis for Marketing*, *17*(2), 139–142. https://doi.org/10.1057/jt.2009.5

Ray, R. D., & Zaron, E. D. (2016). M2 internal tides and their observed wavenumber spectra from satellite altimetry. *Journal of Physical Oceanography*, *46*(1), 3–22. https://doi.org/10.1175/jpo-d-15-0065.1

Rossby, T. (2016). Visualizing and quantifying oceanic motion. *Annual Review of Marine Science*, *8*(1), 35–57. https://doi.org/10.1146/annurev-marine-122414-033849

Sarradin, P. M., & Matabos, M. (2022). *Momarsat 2022 (Tech. Rep.)*. Ifremer. https://doi.org/10.17600/18001914

Smith, K. S., & Vallis, G. K. (2001). The scales and equilibration of midocean eddies: Freely evolving flow. *Journal of Physical Oceanography*, *31*(2), 554–571. https://doi.org/10.1175/1520-0485(2001)031⟨0554:TSAEOM⟩2.0.CO;2

Smith, W. H. F., & Sandwell, D. T. (1997). Global sea floor topography from satellite altimetry and ship depth soundings. *Science*, *277*(5334), 1956–1962. https://doi.org/10.1126/science.277.5334.1956

Steinberg, J. M., & Eriksen, C. C. (2022). Eddy vertical structure and variability: Deepglider observations in the North Atlantic. *Journal of Physical Oceanography*, *52*(6), 1091–1110. https://doi.org/10.1175/JPO-D-21-0068.1

St. Laurent, L., & Garrett, C. (2002). The role of internal tides in mixing the deep ocean. *Journal of Physical Oceanography*, *32*(10), 2882–2899. https://doi.org/10.1175/1520-0485(2002)032⟨2882:TROITI⟩2.0.CO;2

St Laurent, L., & Nash, J. (2004). An examination of the radiative and dissipative properties of deep ocean internal tides. *Deep-Sea Res. II*, *51*(25), 3029–3042. https://doi.org/10.1016/j.dsr2.2004.09.008

Tagliabue, A., Lough, A. J., Vic, C., Roussenov, V., Gula, J., Lohan, M. C., et al. (2022). Mechanisms driving the dispersal of hydrothermal iron from the northern Mid Atlantic Ridge. *Geophysical Research Letters*, *49*(22). https://doi.org/10.1029/2022GL100615

Taylor, R. (1990). Interpretation of the correlation coefficient: A basic review. *Journal of Diagnostic Medical Sonography*, *6*(1), 35–39. https://doi.org/10.1177/875647939000600106

Thoppil, P. G., Richman, J. G., & Hogan, P. J. (2011). Energetics of a global ocean circulation model compared to observations. *Geophysical Research Letters*, *38*(15). https://doi.org/10.1029/2011GL048347

Thurnherr, A., Richards, K., German, C., Lane-Serff, G., & Speer, K. (2002). Flow and mixing in the rift valley of the Mid-Atlantic Ridge. *Journal of Physical Oceanography*, *32*(6), 1763–1778. https://doi.org/10.1175/1520-0485(2002)032⟨1763:FAMITR⟩2.0.CO;2

Tippenhauer, S., Dengler, M., Fischer, T., & Kanzow, T. (2015). Turbulence and finestructure in a deep ocean channel with sill overflow on the mid-Atlantic ridge. *Deep-Sea Research Part I*, *99*, 10–22. https://doi.org/10.1016/j.dsr.2015.01.001

Vic, C., Ferron, B., Thierry, V., Mercier, H., & Lherminier, P. (2021). Tidal and near-inertial internal waves over the Reykjanes Ridge. *Journal of Physical Oceanography*, *51*(2), 419–437. https://doi.org/10.1175/JPO-D-20-0097.1

Vic, C., Gula, J., Roullet, G., & Pradillon, F. (2018). Dispersion of deep-sea hydrothermal vent effluents and larvae by submesoscale and tidal currents. *Deep-Sea Research Part I*, *133*, 1–18. https://doi.org/10.1016/j.dsr.2018.01.001

Vic, C., Naveira Garabato, A. C., Green, J. M., Waterhouse, A. F., Zhao, Z., Melet, A., et al. (2019). Deep-ocean mixing driven by small-scale internal tides. *Nature Communications*, *10*(1), 2099. https://doi.org/10.1038/s41467-019-10149-5

Vic, C., Naveira Garabato, A. C., Green, J. A. M., Spingys, C., Forryan, A., Zhao, Z., & Sharples, J. (2018). The lifecycle of semidiurnal internal tides over the northern Mid-Atlantic Ridge. *Journal of Physical Oceanography*, *48*(1), 61–80. https://doi.org/10.1175/JPO-D-17-0121.1

Walter, M., Mertens, C., Stöber, U., German, C. R., Yoerger, D. R., Sültenfuß, J., et al. (2010). Rapid dispersal of a hydrothermal plume by turbulent mixing. *Deep-Sea Research Part I*, *57*(8), 931–945. https://doi.org/10.1016/j.dsr.2010.04.010

Wang, S., Cao, A., Chen, X., Li, Q., & Song, J. (2021). On the resonant triad interaction over mid-ocean ridges. *Ocean Modelling*, *158*, 101734. https://doi.org/10.1016/j.ocemod.2020.101734

Whalen, C. B., de Lavergne, C., Naveira Garabato, A. C., Klymak, J. M., MacKinnon, J. A., & Sheen, K. L. (2020). Internal wave-driven mixing: Governing processes and consequences for climate. *Nature Reviews Earth and Environment*, *1*(11), 606–621. https://doi.org/10.1038/s43017-020-0097-z

Wunsch, C. (2015). *Modern observational physical oceanography: Understanding the global ocean*. Princeton University Press.

Yang, C.-F., Chi, W.-C., & van Haren, H. (2021). Deep-sea turbulence evolution observed by multiple closely spaced instruments. *Scientific Reports*, *11*(1), 3919. https://doi.org/10.1038/s41598-021-83419-2

Yu, X., Ponte, A. L., Elipot, S., Menemenlis, D., Zaron, E. D., & Abernathey, R. (2019). Surface kinetic energy distributions in the global oceans from a high-resolution numerical model and surface drifter observations. *Geophysical Research Letters*, *46*(16), 9757–9766. https://doi.org/10.1029/2019gl083074

Zaron, E. D., & Egbert, G. D. (2014). Time-variable refraction of the internal tide at the Hawaiian Ridge. *Journal of Physical Oceanography*, *44*(2), 538–557. https://doi.org/10.1175/JPO-D-12-0238.1

Zilberman, N., Becker, J., Merrifield, M., & Carter, G. (2009). Model estimates of M_2 internal tide generation over Mid-Atlantic Ridge topography. *Journal of Physical Oceanography*, *39*(10), 2635–2651. https://doi.org/10.1175/2008JPO4136.1

Zweng, M., Reagan, J., Seidov, D., Boyer, T., Locarnini, R., Garcia, H., et al. (2018). *World Ocean Atlas 2018, volume 2: Salinity* (Vol. 82, p. 50). NOAA Atlas NESDIS. Retrieved from https://data.nodc.noaa.gov/woa/WOA18/DOC/woa18_vol2.pdf